

On the Climatology of Precipitable Water and Water Vapor Flux in the Mid-Atlantic Region of the United States

YOUNG-HEE RYU, JAMES A. SMITH, AND ELIE BOU-ZEID

Department of Civil and Environmental Engineering, Princeton University, Princeton, New Jersey

(Manuscript received 19 February 2014, in final form 12 July 2014)

ABSTRACT

The seasonal and diurnal climatologies of precipitable water and water vapor flux in the mid-Atlantic region of the United States are examined. A new method of computing water vapor flux at high temporal resolution in an atmospheric column using global positioning system (GPS) precipitable water, radiosonde data, and velocity–azimuth display (VAD) wind profiles is presented. It is shown that water vapor flux exhibits striking seasonal and diurnal cycles and that the diurnal cycles exhibit rapid transitions over the course of the year. A particularly large change in the diurnal cycle of meridional water vapor flux between spring and summer seasons is found. These features of the water cycle cannot be resolved by twice-a-day radiosonde observations. It is also shown that precipitable water exhibits a pronounced seasonal cycle and a less pronounced diurnal cycle. There are large contrasts in the climatology of water vapor flux between precipitation and nonprecipitation conditions in the mid-Atlantic region. It is hypothesized that the seasonal transition of large-scale flow environments and the change in the degree of differential heating in the mountainous and coastal areas are responsible for the contrasting diurnal cycle between spring and summer seasons.

1. Introduction

Water vapor in the atmosphere plays critical roles in cloud formation, precipitation, and the atmospheric radiation budget. The correct initialization of atmospheric water vapor, for example, directly affects the forecast accuracy of precipitation in terms of occurrence and amount (Hanesiak et al. 2010). Water vapor also plays a central role in analyses of Earth's climate, especially in connection with the response of the climate system to warming (Held and Soden 2006). In this study, we examine the climatology of atmospheric water vapor in the mid-Atlantic region of the United States, with a special focus on the diurnal and seasonal cycles of precipitable water and vertically integrated water vapor flux. The mid-Atlantic region of the United States is adjacent to the Atlantic Ocean to the east in midlatitudes.

Since the 1990s, the total mass of water vapor in an atmospheric column, that is, the precipitable water, has been derived at high temporal resolution (30 min) from ground-based global positioning system (GPS) measurements

(e.g., Bevis et al. 1994). Radiosonde observations that are traditionally used for atmospheric water vapor analyses have poor temporal resolution (12 h) for resolving diurnal variations in atmospheric water vapor. The GPS-derived precipitable water data have the advantages of continuous measurements with high temporal resolution, availability under all weather conditions, and high accuracy (Wang et al. 2007). The high temporal resolution of GPS observations provides an opportunity to improve our understanding of the diurnal cycle in atmospheric water vapor as well as its seasonal cycle. Analyses of GPS precipitable water data have provided important new insights into the climatology of precipitable water over the world (e.g., Dai and Wang 2002; Wu et al. 2003; Wang et al. 2007; Hanesiak et al. 2010).

The amount of water vapor at a location is greatly affected by atmospheric transport as well as local evaporation and condensation. To understand the atmospheric water cycle, it is critical to understand climatological properties of water vapor flux, which depend on both the vertical profile of the horizontal wind and the vertical profile of humidity. Because of the concentration of water vapor in the lower troposphere, climatological properties of the low-level winds are most important for assessing water vapor transport. The monthly and seasonal variations in water vapor flux over North America (Benton and

Corresponding author address: Young-Hee Ryu, Department of Civil and Environmental Engineering, Princeton University, Princeton, NJ 08544.
E-mail: younghee@princeton.edu

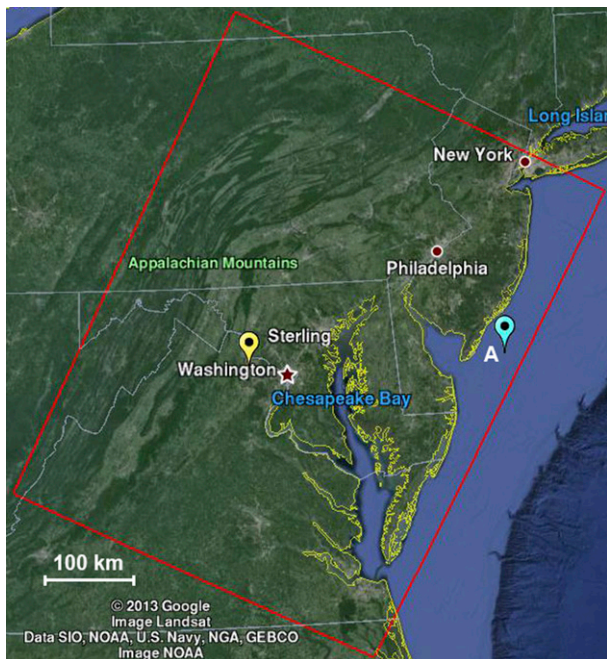


FIG. 1. Geographical map of the study area. Sterling, Virginia, in which the GPS, radiosonde, and radar stations are collocated, is marked with the yellow-dot balloon. Point A, which is used in the temperature analysis in Fig. 19, is marked with the blue-dot balloon. Several major cities in the mid-Atlantic region are denoted by the red markers. The area marked with red lines is used when area-averaged precipitation is computed.

Estoque 1954; Rasmusson 1967) have been examined using observations from the radiosonde network. The diurnal variation in water vapor flux over North America (Rasmusson 1967) has been examined using radiosonde observations for special observation periods. Radiosonde observations have the advantage of combined measurements of water vapor and horizontal winds, providing the foundation for assessing water vapor flux. As noted above, however, radiosonde observations have the drawback of poor temporal resolution, which is particularly important for water vapor flux (as detailed below). In this study, we present a new method of computing water vapor flux at high temporal resolution using GPS precipitable water observations, velocity–azimuth display (VAD) wind profiles derived from a Doppler radar, and radiosonde observations.

The objectives of this study are to present a new method for computing water vapor flux and to analyze the climatology of precipitable water and of vertically integrated water vapor flux. The study area is the mid-Atlantic region of the United States, and analyses are designed to provide insights into the water cycle over the eastern megalopolis of the United States.

The mid-Atlantic region (see Fig. 1 for a geographical map) is an interesting and complex setting for examining

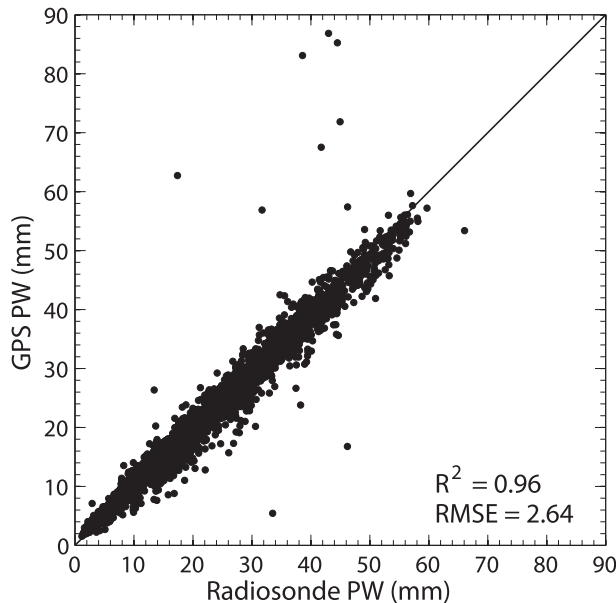


FIG. 2. Scatterplot of precipitable water observed from GPS and radiosonde at Sterling for 2007–12.

the atmospheric water cycle. The geographical features of the study region can be characterized by sloping terrain from the Appalachian Mountains in the west and by land–ocean contrast due to the Atlantic Ocean in the east. The study region is subject to local circulations such as mountain–valley circulation and land–sea breeze circulation and also low-level jets. Because the diurnal variation in water vapor transport can be associated with the diurnal variation in wind (Rasmusson 1967), it is important to understand local wind systems and their

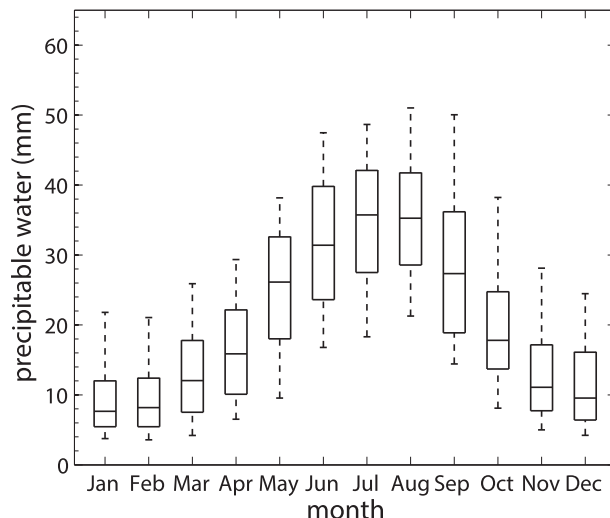


FIG. 3. Monthly box plots of precipitable water. The central mark on each box indicates the median, and the bottom (top) edge of each box indicates the 25th (75th) percentile. Whiskers (vertical bars) represent the range from the 5th to the 95th percentiles of the data.

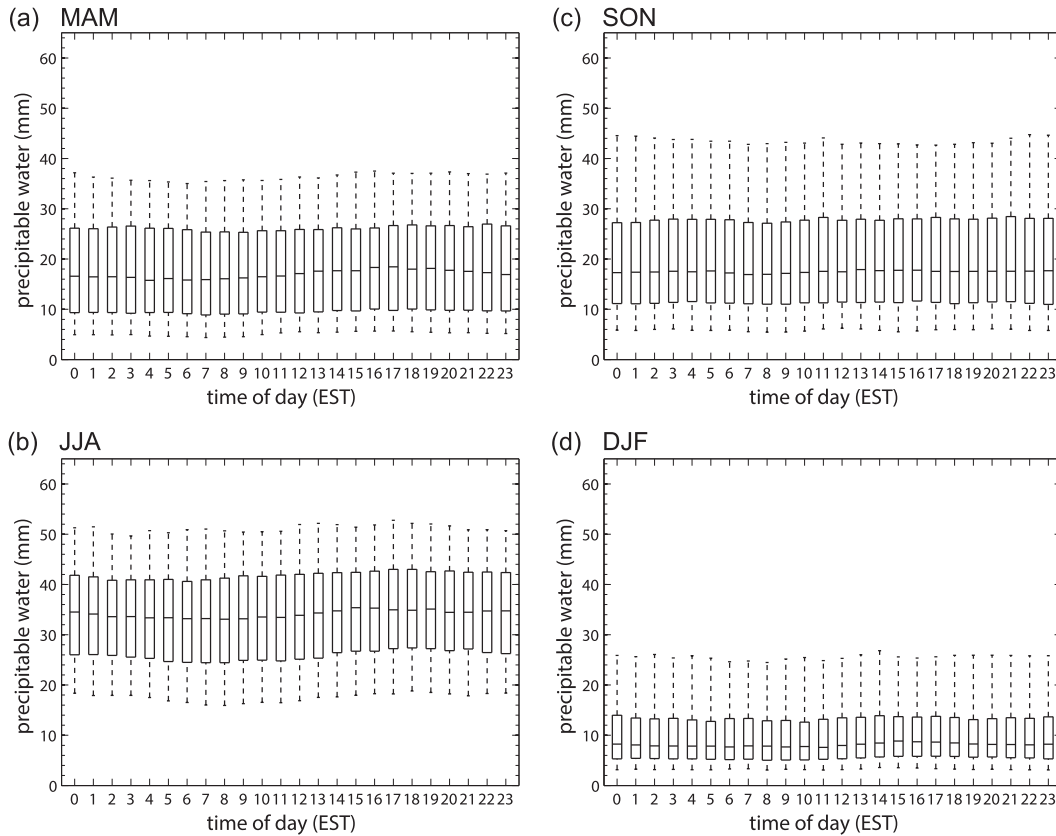


FIG. 4. Hourly box plots of precipitable water in (a) spring (March–May), (b) summer (June–August), (c) autumn (September–November), and (d) winter (December–February).

climatological characteristics. It has been demonstrated that nocturnal low-level jets can develop in the mid-Atlantic region (e.g., Sjostedt et al. 1990; Zhang et al. 2006; Colle and Novak 2010). As in the Great Plains, the sloping terrain due to the Appalachian Mountains together with the thermal contrasts between land and the Atlantic Ocean can induce a thermal wind oscillation (Colle and Novak 2010). Zhang et al. (2006) observed the frequent occurrence of nocturnal low-level jets following the orientation of the Appalachian Mountains. Colle and Novak (2010) reported that the northward New York Bight jets develop primarily during the warm seasons in the mid-Atlantic and northeastern U.S. coastal regions.

A detailed description of the new method for computing water vapor flux is given in section 2. In section 3, we present and analyze the seasonal and diurnal climatology of precipitable water and water vapor flux. A discussion of our findings is given in section 4, and a summary and conclusions are given in section 5.

2. Data and methods

Precipitable water can be represented in terms of the vertical profile of water vapor density as follows:

$$W = \int_0^{z_t} \rho_v(z) dz, \quad (1)$$

where the upper limit z_t typically denotes the elevation of the top of the troposphere (we will focus on a lower limit of integration, as detailed below). The precipitable water has units of kilogram per square meter. Dividing by the density of water (1000 kg m^{-3}) and multiplying by 1000 mm m^{-1} , we see that the precipitable water can also be expressed in units of millimeters.

The vertically integrated water vapor flux vector $\mathbf{Q} = (Q_x, Q_y)$ is defined as follows:

$$Q_x = \int_0^{z_{\text{top}}} \rho_v(z) u(z) dz \quad (2)$$

and

$$Q_y = \int_0^{z_{\text{top}}} \rho_v(z) v(z) dz, \quad (3)$$

where $u(z)$ is the zonal (east–west) component of the wind (m s^{-1} ; positive eastward) at elevation z and $v(z)$ is the meridional (north–south) component of the wind

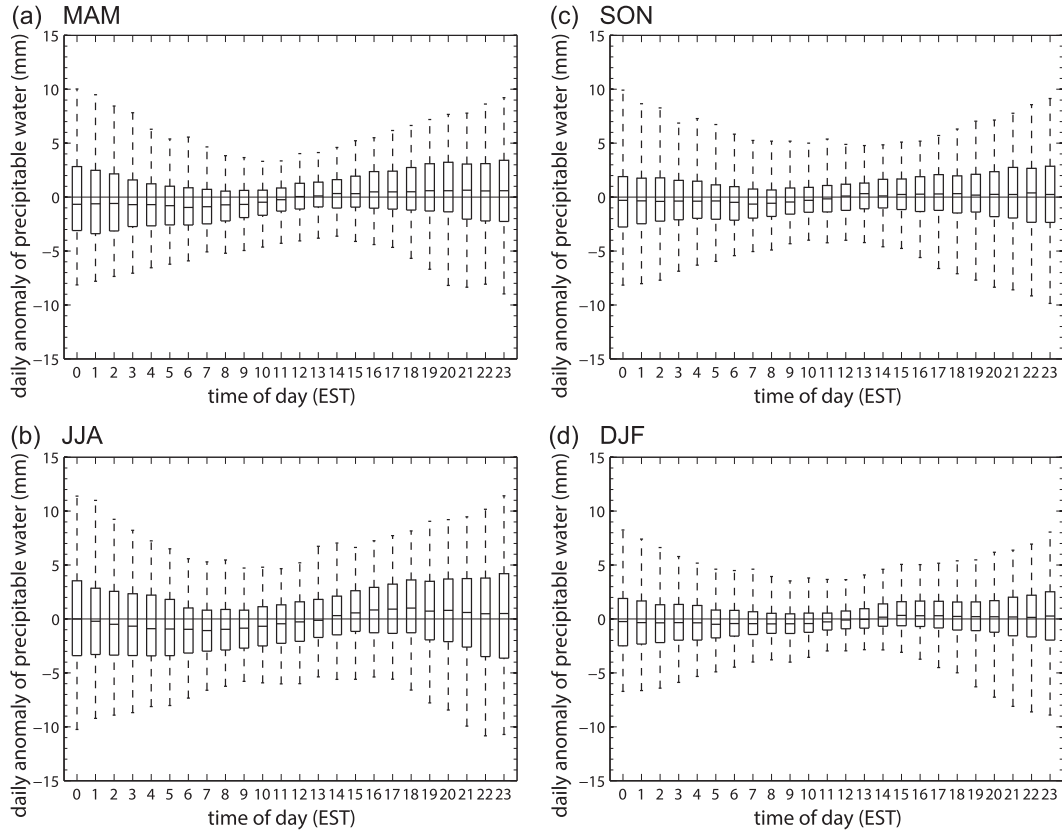


FIG. 5. Hourly box plots of daily anomaly of precipitable water in (a) spring, (b) summer, (c) autumn, and (d) winter.

(m s^{-1} ; positive northward) at elevation z . The mass flux of water vapor across a plane of unit width in the north–south direction extending to z_{top} (Q_x) and a plane of unit width in the east–west direction extending to z_{top} (Q_y) is given by Q_x and Q_y ($\text{kg m}^{-1} \text{s}^{-1}$).

We will denote the precipitable water at time t ($t \in 0\text{--}24$) on day i of the year by $W_i(t)$; the water vapor flux vector at time t on day i will be denoted $[Q_x^i(t), Q_y^i(t)]$. GPS precipitable water time series are constructed (interpolated) at 15-min time steps using the original data with 30-min time resolution for the Sterling, Virginia, study site (Fig. 1) during the period from 2007 to 2012. GPS precipitable water time series provide samples of $[W_i(t); t \in (0\text{--}24), i = 1, \dots, 365]$ for each year of 2007–12. VAD wind profiles are derived from the Weather Surveillance Radar-1988 Doppler (WSR-88D) radar at Sterling, Virginia (KLWX). VAD wind profiles are computed at volume scan times (typically 5–10 min) and converted to a regular 15-min time interval and a vertical spacing of 50 m. Radiosonde observations (at 0000 and 1200 UTC) are obtained from Dulles International Airport (KIAD) in Sterling, Virginia, for the period from 2007 to 2012.

We compute water vapor flux time series at 15-min time interval during the time period from 2007 to 2012

from GPS precipitable water observations, radiosonde profiles of water vapor density at 0000 and 1200 UTC, and VAD wind profiles at 15-min time interval. The VAD wind profiles are used directly to compute $[u_i(t, z), v_i(t, z)]$ needed to compute the time series of water vapor flux [Eqs. (2) and (3)].

The time series of water vapor density profiles $\rho_v^i(t, z)$ are computed under the assumption that the profile of normalized water vapor density, that is, water vapor density divided by precipitable water, is slowly varying over the course of the day and can be estimated from twice-a-day radiosonde profiles. Normalized water vapor density profiles are computed from radiosonde data at time t_1 (0000 UTC) and t_2 (1200 UTC) as

$$f^i(t_j, z) = \frac{\rho_v^i(t_j, z)}{W_i(t_j)} \quad (4)$$

for j equal to 1 or 2. Here, $W_i(t_j)$ is the precipitable water from the radiosonde measurement. The normalized water density profile is computed at an arbitrary time during day i as a weighted sum of the two advanced normalized profiles:

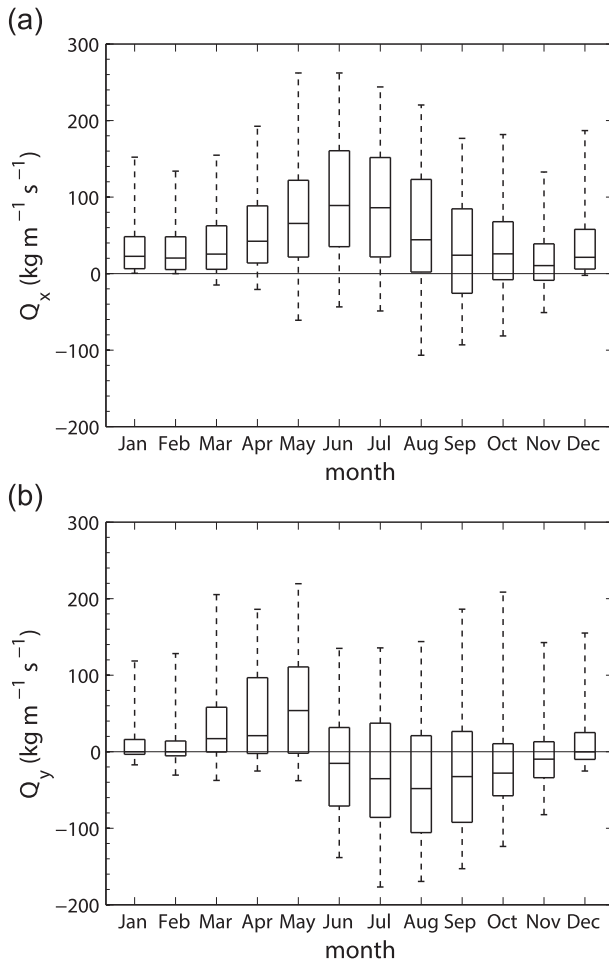


FIG. 6. Monthly box plots of vertically integrated (a) zonal and (b) meridional water vapor flux.

$$f^i(t, z) = \alpha f^i(t_1, z) + (1 - \alpha) f^i(t_2, z), \quad (5)$$

where the weight α provides a linear average of the two adjacent profiles as a function of the time difference between t and t_2 [i.e., $\alpha = (t_2 - t)/(t_2 - t_1)$]. Then, the water vapor density profile at an arbitrary time t during day i is computed from the GPS precipitable water at time t and the normalized water vapor density profile:

$$\rho_v^i(t, z) = f^i(t, z)[W_i(t)]. \quad (6)$$

Therefore, the water vapor flux profile and vertically integrated water vapor flux at an arbitrary time t during day i can be computed using $\rho_v^i(t, z)$ and the wind vector $[u_i(t, z), v_i(t, z)]$.

In this study, data from the North American Regional Reanalysis (NARR; Mesinger et al. 2006) are used to analyze the large-scale flow environments that are associated with water vapor transport and to compare with the

observation data. NARR is produced at 32-km resolution in the horizontal and 3-h temporal resolution. There are 13 vertical layers below 700 hPa with an interval of 25 hPa. The time period used for NARR is the same as that for observations, which is from 2007 to 2012.

3. Results

a. Precipitable water climatology

Precipitable water observed from GPS at Sterling closely matches precipitable water measurements derived from radiosonde observations at the same site (Fig. 2). Since the radiosonde data are only available twice a day (0000 and 1200 UTC), the corresponding GPS data at 0000 and 1200 UTC are compared. The relationship between the two datasets is characterized by an R^2 of 0.96 and a root-mean-square error of 2.64 mm [see Dai and Wang (2002) for detailed assessments of the accuracy of GPS precipitable water data].

The monthly variation in daily mean GPS precipitable water (Fig. 3) shows a pronounced seasonal variation with maxima in summer months and minima in winter months. The median precipitable water ranges from 7.7 (January) to 35.7 mm (July). In warm months (May–September), the precipitable water shows a larger variability than in cold months.

The diurnal variation in precipitable water (Fig. 4) exhibits large variability in all seasons, as reflected in the interquartile range of hourly precipitable water. The median precipitable water shows a weak diurnal cycle with an amplitude of ~ 1 mm in spring and summer and a much weaker variation in autumn and winter. The diurnal amplitudes of median precipitable water in spring, summer, autumn, and winter are 1.3, 1.1, 0.5, and 0.6 mm, respectively. The magnitude of the amplitudes in spring and summer, ~ 1 mm, is similar to that reported in previous studies (Dai and Wang 2002; Wu et al. 2003; Hanesiak et al. 2010). For example, Dai and Wang (2002) showed that the diurnal cycle of precipitable water has an amplitude of 1.0–1.8 mm over most of the central and eastern United States during summer.

The median values of precipitable water reach a maximum in the afternoon and a minimum in the morning for all seasons, which is also consistent with the previous studies. The diurnal cycle is more clearly seen in the daily anomaly of precipitable water (Fig. 5), particularly in spring and summer. The precipitable water anomaly is computed as the instantaneous value during the day minus the mean value for the day (Dai and Wang 2002). The variability in precipitable water anomaly exhibits a more pronounced diurnal cycle with a peak variability at around 2300 Eastern Standard Time (EST) and a minimum

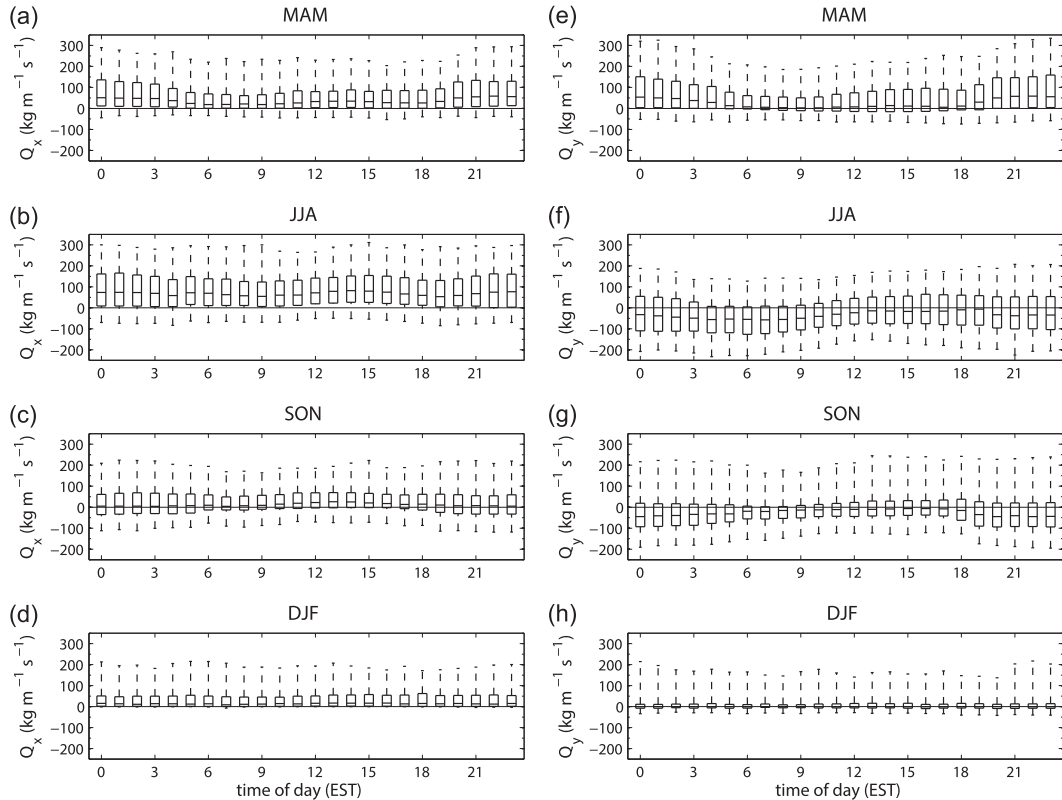


FIG. 7. Hourly box plots of vertically integrated (left) zonal and (right) meridional water vapor flux in (a),(e) spring; (b),(f) summer; (c),(g) autumn; and (d),(h) winter.

variability at around 0900 EST. This diurnal cycle of variability is similarly observed in all seasons. Although the precipitable water exhibits diurnal variation, the degree of the variation is small relative to its magnitude and variability. The ratio of the amplitude to the median in spring, summer, autumn, and winter is 7.2%, 3.2%, 2.6%, and 7.1%, respectively.

b. Water vapor flux analyses

Analyses of water vapor flux focus on vertically integrated values up to 3 km above ground level (AGL). The 3-km elevation captures the dominant transport of water vapor in the lower atmosphere and also utilizes VAD winds over the extent of the atmosphere for which they are reliably available.

The vertically integrated zonal water vapor flux (i.e., Q_x) shows a pronounced seasonal variation with maxima in summer months and minima in winter months (Fig. 6a). The median values of zonal water vapor flux reach a maximum of $89.0 \text{ kg m}^{-1} \text{ s}^{-1}$ in June and a minimum of $10.4 \text{ kg m}^{-1} \text{ s}^{-1}$ in November. The median value of the zonal water vapor flux is positive for all months, indicating eastward transport of water vapor in all seasons. This seasonal variation is attributed to the seasonal variation in

water vapor density rather than to variation in zonal wind. The zonal wind is much stronger in winter months than in summer months (not shown). On the other hand, the water vapor density is much higher in summer months than in winter months, as can be inferred from the seasonal variation in precipitable water (Fig. 3). The large variability in zonal water vapor flux in summer months is also attributed to the large variability in water vapor density, as can be inferred from the large variability in precipitable water in summer months. The seasonal variability in zonal wind is relatively small (not shown).

The vertically integrated meridional water vapor flux (i.e., Q_y) shows a striking seasonal variation (Fig. 6b). The direction of Q_y changes from northward (positive sign) in spring to southward (negative sign) in summer and autumn (in terms of the median value of the meridional water vapor flux). The interquartile range in spring indicates that the northward transport of water vapor prevails in spring. The northward transport is enhanced in May compared to April. The interquartile range in summer indicates that the water vapor can be transported either from the north or the south, with southward transport more common. The southward transport reaches a peak in August (in terms of the median value).

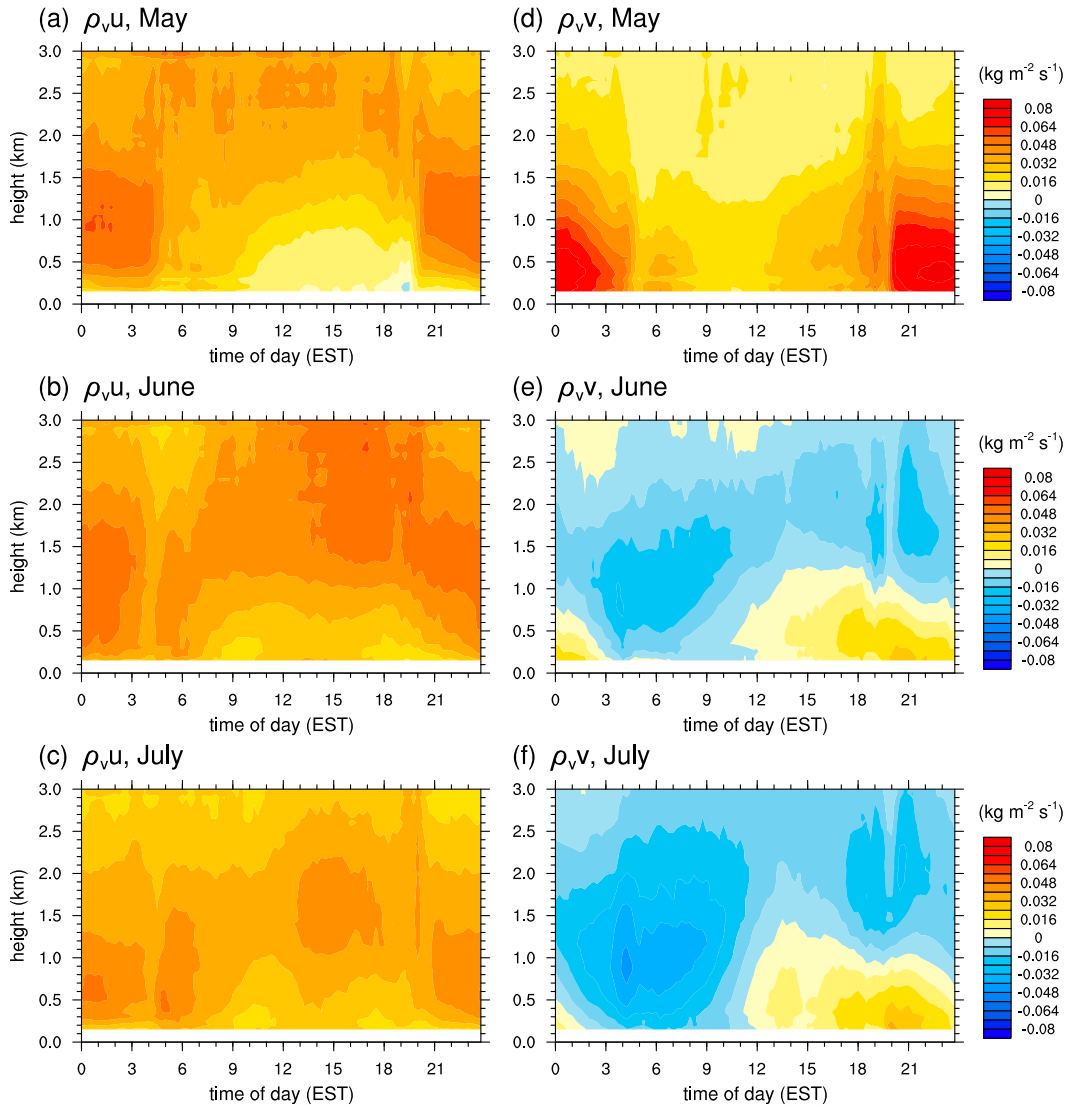


FIG. 8. Time–height cross section of (left) zonal and (right) meridional water vapor flux in (a),(d) May; (b),(e) June; and (c),(f) July.

The zonal transport of water vapor in spring is always dominated by eastward transport over the entire day, and it exhibits a weak diurnal variation in which the zonal water vapor flux is slightly stronger during the nighttime hours than during the daytime hours (Fig. 7a). The vertically integrated meridional water vapor flux has positive (northward transport) median values over the entire day, and it exhibits a more pronounced diurnal variation in which the meridional transport is stronger during the nighttime hours than during the daytime hours (Fig. 7e). It is also seen that the variability in both the fluxes is considerably larger in the nighttime than in the daytime. The enhanced nighttime transport of water vapor in the meridional direction is associated with the low-level jets in the mid-Atlantic region. We

present further analysis and discussion in the latter part of this section and in the discussion section.

In summer, unlike in spring, the vertically integrated zonal water vapor flux exhibits little diurnal variation (but it is always dominated by eastward transport over the entire day) and the nighttime enhancement is not as clearly seen (Fig. 7b). As can be seen in Fig. 6a, the magnitude and variability are largest in summer. The negative median values of vertically integrated meridional water vapor flux indicate that southward transport dominates over the entire day (Fig. 7f). There is, however, a significant diurnal variation in Q_y with median values ranging from $-57.4 \text{ kg m}^{-1} \text{ s}^{-1}$ at 0700 EST to $-6.2 \text{ kg m}^{-1} \text{ s}^{-1}$ at 1900 EST. The northward transport of water vapor still occurs during the afternoon and evening hours, and this

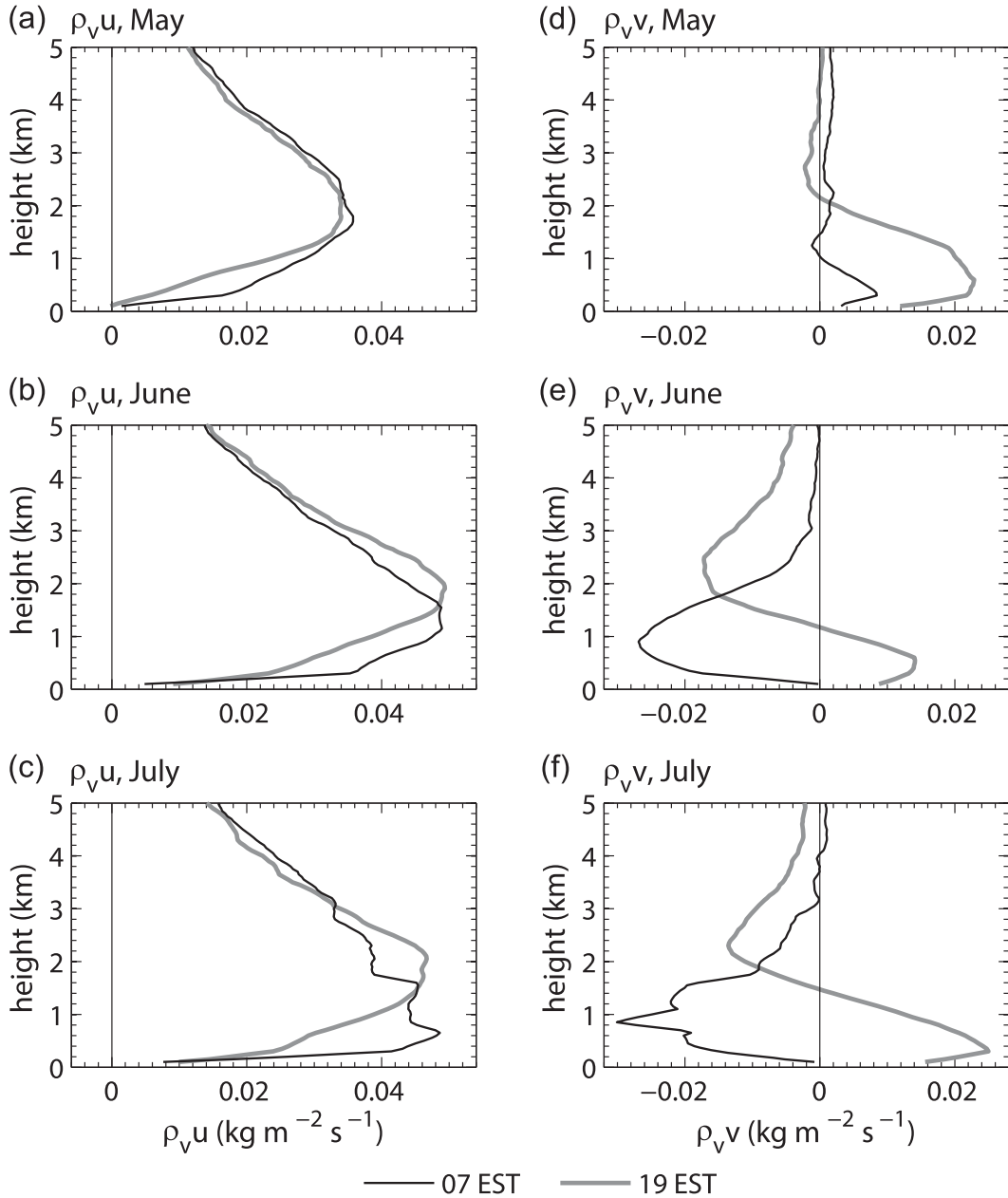


FIG. 9. Vertical profiles of (left) zonal and (right) meridional water vapor flux in (a),(d) May; (b),(e) June; and (c),(f) July derived from radiosonde observations at Sterling for 2007–12.

northward transport explains the positive Q_y in summer in Fig. 6b.

In autumn, the magnitude and the variability of vertically integrated zonal water vapor flux are reduced compared to those in summer (Fig. 7c). Unlike in spring and summer in which eastward water vapor flux predominates both in the day- and nighttime, the transport of water vapor from the east as well as from the west is observed in the nighttime. So, the negative interquartile range in Q_x in autumn (Fig. 6a) is attributed to the

westward water vapor flux during the nighttime. The nighttime southward water vapor flux becomes more predominant in autumn than in summer (Fig. 7g). The reduced interquartile range of vertically integrated water vapor flux is attributed to the decreases in magnitude and variability in water vapor density. In winter, both the zonal and meridional water vapor fluxes are greatly reduced (Figs. 7d,h). As in autumn, the small interquartile range of the water vapor fluxes results from the reduction in water vapor density (or precipitable water) rather than

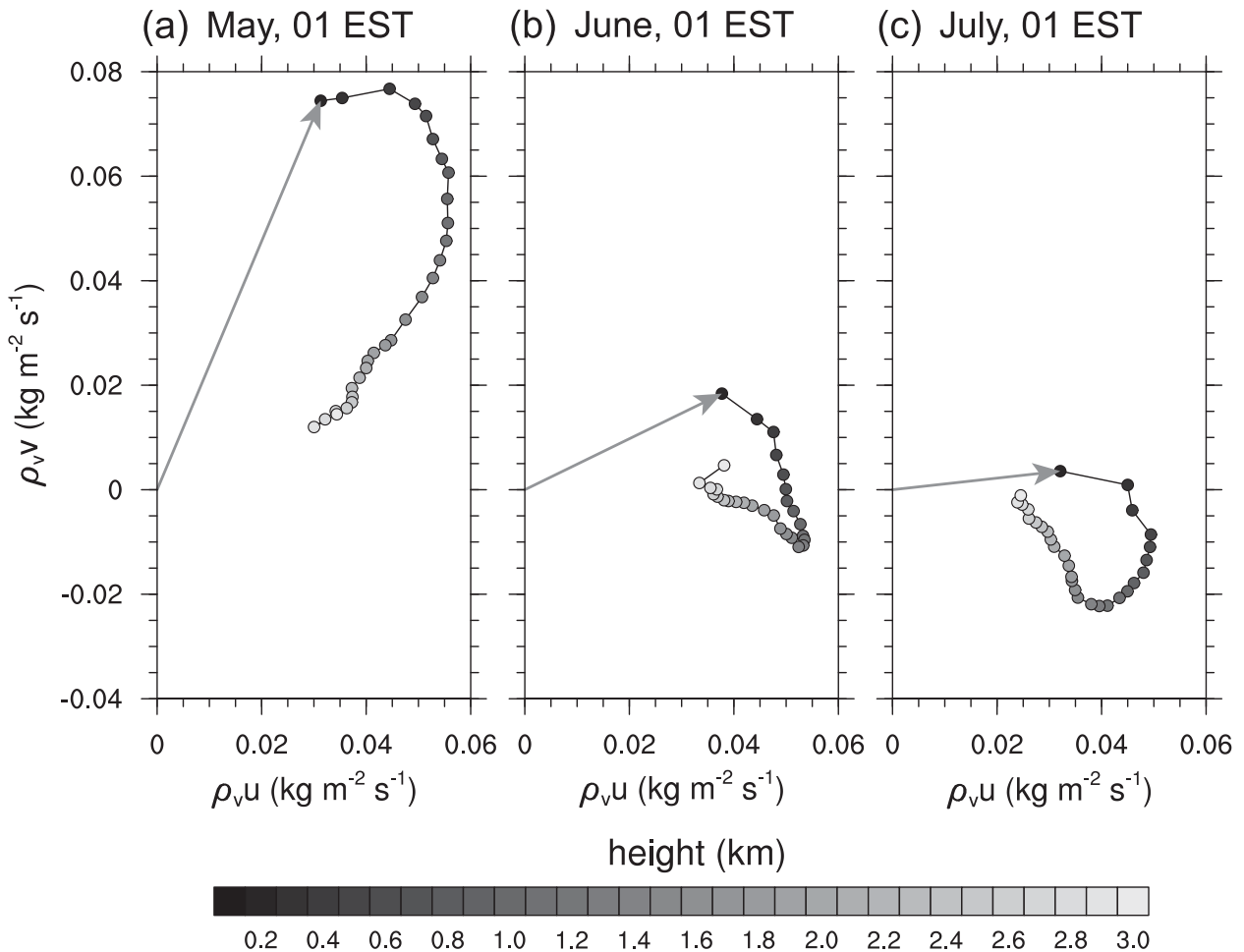


FIG. 10. Hodographs of (ρ_{vu}, ρ_{vv}) for Sterling at 0100 EST (a) May, (b) June, and (c) July. The vertical levels (km AGL) are represented by different shading.

from the wind. The variabilities in zonal and meridional winds are comparable (or even larger) in autumn and winter than in spring and summer (not shown).

One of the key findings of this study is that the vertically integrated meridional water vapor flux exhibits very different diurnal variations between spring and summer. To investigate this transition between spring and summer, time–height cross sections of water vapor flux in May, June, and July are presented in Fig. 8. During May (Figs. 8a,d), the enhanced northeastward water vapor flux in the nighttime is clearly seen at low levels (below ~ 1 km) and weak northeastward flux is seen during the middle of the day. Vertical gradients in meridional transport of water vapor are large at night with the low-level transport maximum of $0.084 \text{ kg m}^{-2} \text{ s}^{-1}$ at 0.35 km AGL at 2300 EST decreasing to about one-tenth of the maximum value at 3 km AGL. An abrupt time transition of vertical profile of water vapor flux occurs at ~ 2000 EST and a similar but less pronounced transition

occurs at 0400–0500 EST for May. These transitions are attributed to some extent to missing data that are more frequent at ~ 1800 – 1900 EST and at ~ 0500 – 0700 EST for May. For example, in May, the ratio of missing data at 0.5 km AGL during 0500–0700 and 1800–1900 EST periods is $\sim 15\%$, while during the rest of the time periods it is $\sim 6\%$. The meridional water vapor flux during summer shows a contrasting diurnal variation in which southeastward flux dominates during the nighttime hours and northeastward flux dominates during the afternoon and evening hours at low levels. As noted above, even in summer season, the northward transport of water vapor is observed at low levels during afternoon and evening hours, and this transport reaches a peak at 2030 EST in June and at 2000 EST in July, but the vertical gradients are not as strong as in May.

The vertical profiles of water vapor flux obtained from Sterling radiosonde in May, June, and July (Fig. 9) match well with the results based on GPS precipitable water and

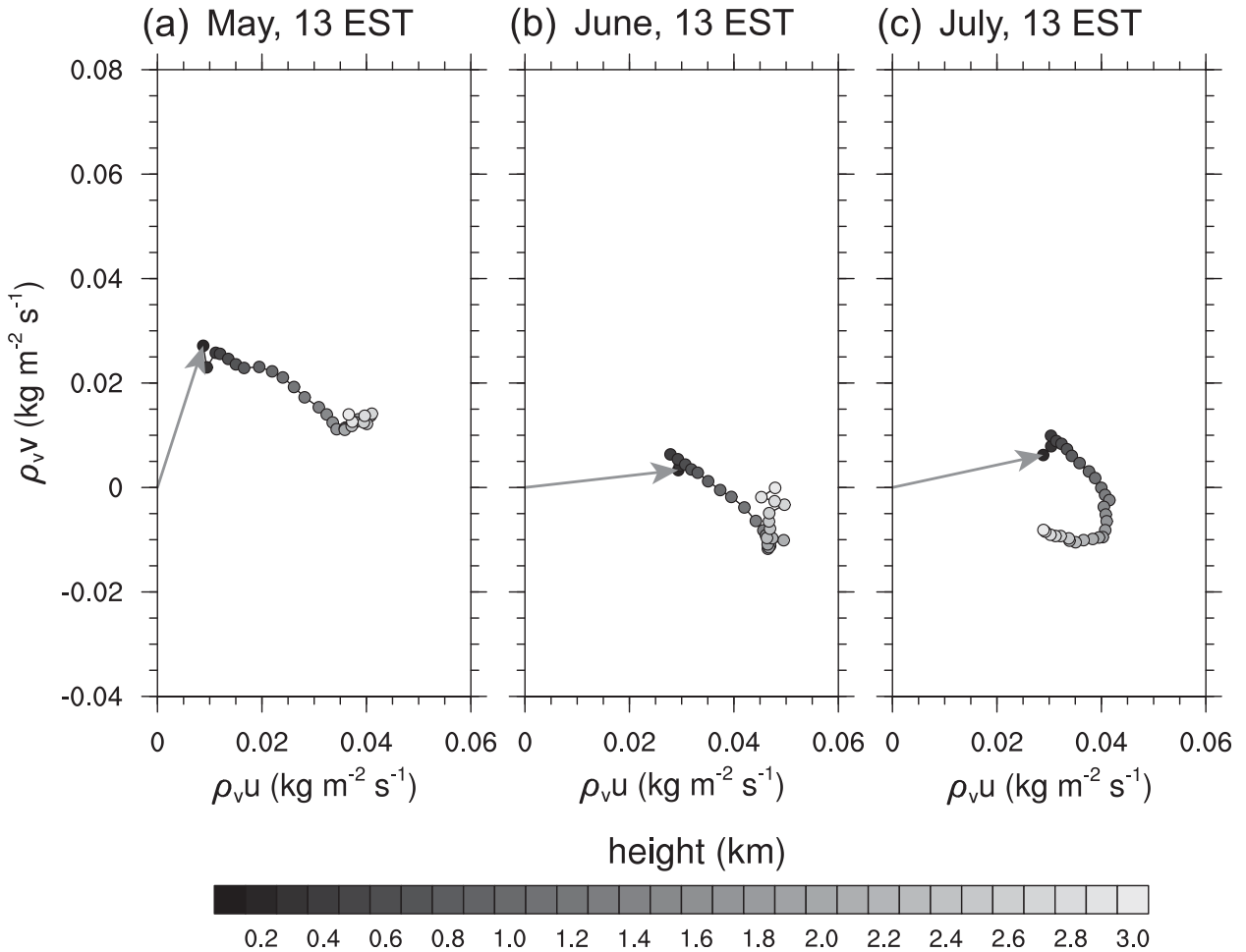


FIG. 11. As in Fig. 10, but for 1300 EST.

VAD wind profiles and show consistent results for the seasonal transition of diurnal variation in water vapor flux between spring and summer seasons. During May (Figs. 9a,d), the zonal water vapor flux reaches a peak at ~ 2 km, and the meridional water vapor flux is northward at both 0700 and 1900 EST at low levels and stronger at 1900 EST. During June and July (Figs. 9e,f), the meridional water vapor flux shows consistent results in which it is southward at 0700 EST and northward at 1900 EST at low levels. Although it is not highlighted in Rasmusson (1967), a similar change in water vapor flux between 1200 UTC (0700 EST) and 0000 UTC (1900 EST) for June–August in 1961 and 1962 was observed in the mid-Atlantic region. It was shown that the mean differential vertically integrated water vapor flux between 0700 and 1900 EST (i.e., 0700 minus 1900 EST) is southeastward in the mid-Atlantic region, which is consistent with our analysis results. However, the pronounced diurnal and vertical variation of water vapor flux cannot be resolved by twice-a-day radiosonde observations.

Mean hodographs of $(\rho_v u, \rho_v v)$ at 0100 EST at 0.1-km vertical intervals in May, June, and July (Fig. 10) illustrate the vertical structure of water vapor flux. The time 0100 EST is chosen as a representative nighttime. During May (Fig. 10a), the water vapor flux veers with height from northeastward near the surface to east-northeastward at upper levels ($z > \sim 1.5$ km). As seen in Fig. 8, the water vapor flux at 0100 EST in June and July is east-northeastward near the surface but changes to southeastward at 0.7 km AGL in June and at 0.3 km in July. The water vapor flux at 0100 EST reaches a local maximum at 0.5 km AGL in May and 0.4 km in June and July, and this can be explained by the inertial oscillation theory of Blackadar (1957). An inertial oscillation can lead to a maximum wind speed above the top of the nocturnal inversions as the former daytime mixed layer rapidly becomes decoupled from the surface and thus the frictional force becomes negligible (Baas et al. 2009). At 1300 EST as a representative daytime (Fig. 11), northeastward water vapor flux is still observed over the

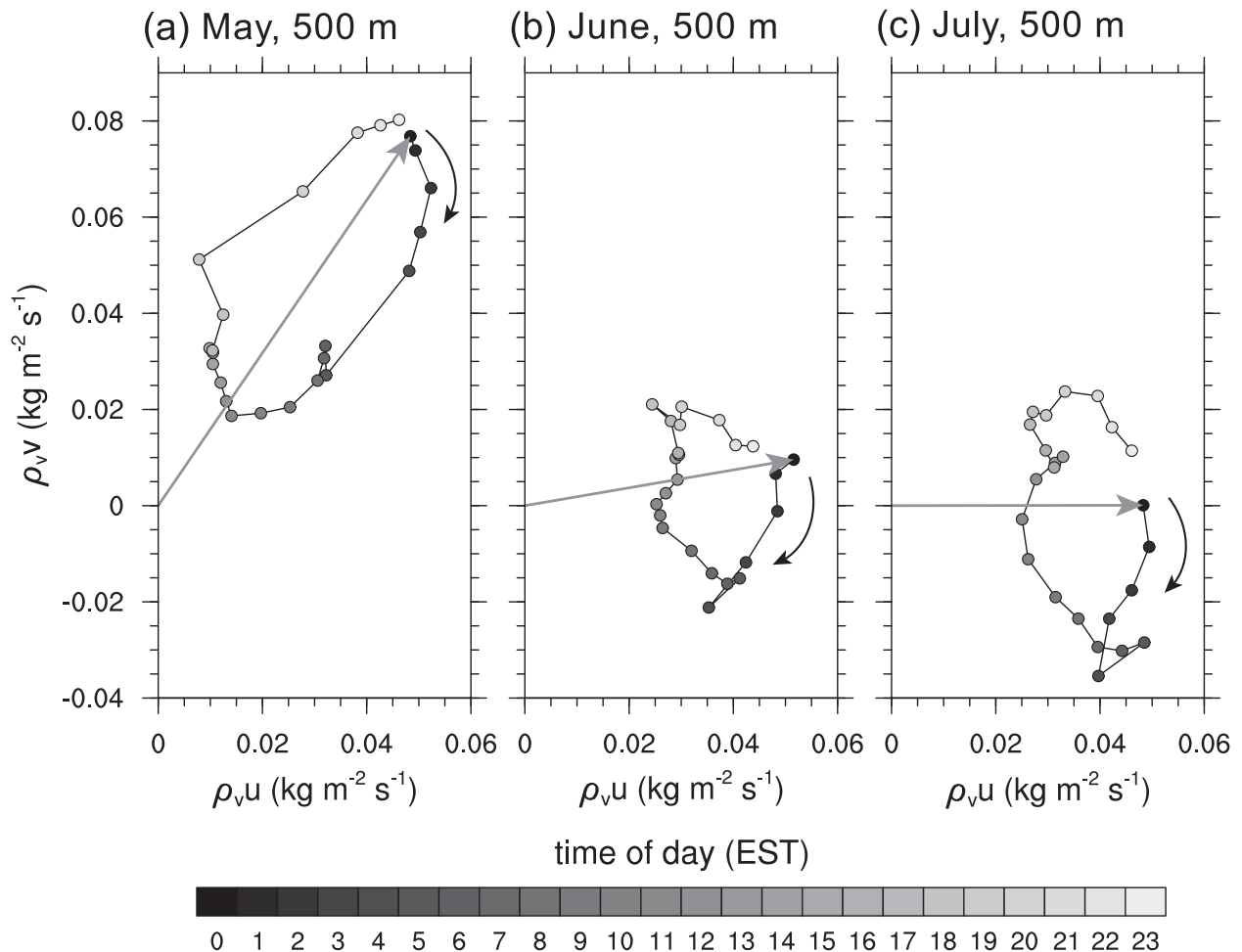


FIG. 12. Hodographs of $(\rho_v u, \rho_v v)$ for Sterling at 0.5 km AGL in (a) May, (b) June, and (c) July. The time of day (EST) is represented by different shading. The curved arrow indicates the clockwise rotation.

entire 3-km layer during May. As in the nighttime, the water vapor flux in June and July changes to southeastward at around 1 km AGL in the daytime. These night- and daytime hodographs of water vapor flux indicate that there is a transition of the upper-level winds (nearly geostrophic winds) from northeastward in May to southeastward in June and July.

Mean hodographs of $(\rho_v u, \rho_v v)$ at 0.5 km AGL in May, June, and July illustrate the diurnal cycle of water vapor flux (Fig. 12). In Fig. 12a, the water vapor flux at 0.5 km AGL reveals a clockwise rotation with time. Thus, during May, the strong northeastward water vapor flux during the nighttime hours can be attributed to some extent to an inertial oscillation. During June and July, the water vapor flux also reveals a clockwise rotation but with smaller amplitude than May. It should be noted that hodographs of horizontal wind (u, v) show similar oscillation patterns with those of water vapor flux ($\rho_v u, \rho_v v$). In addition to the inertial oscillation, the oscillation

in thermal wind that arises from diurnal heating/cooling cycle over sloping terrain and/or over coastal region can lead to the diurnal oscillation in low-level winds (e.g., Bonner and Paegle 1970; Doyle and Warner 1991; Burk and Thompson 1996). Considering the warmer air over mountain slopes compared to the air at the same level to the east during the day [e.g., as given in Bonner and Paegle (1970)] the thermal wind under such circumstances is southward. So, if the upper-level geostrophic winds are northward (e.g., in spring), then the low-level geostrophic winds (equal to the upper-level geostrophic winds minus the thermal winds) become stronger northward winds. Thus, the transition of upper-level winds from northeastward in spring to southeastward in summer may result in a decrease in the northward component of low-level winds during the nighttime hours. At the upper level (1.7 km AGL; Fig. 13), such oscillation is much less clear in May, June, and July. As noted above, the northeastward

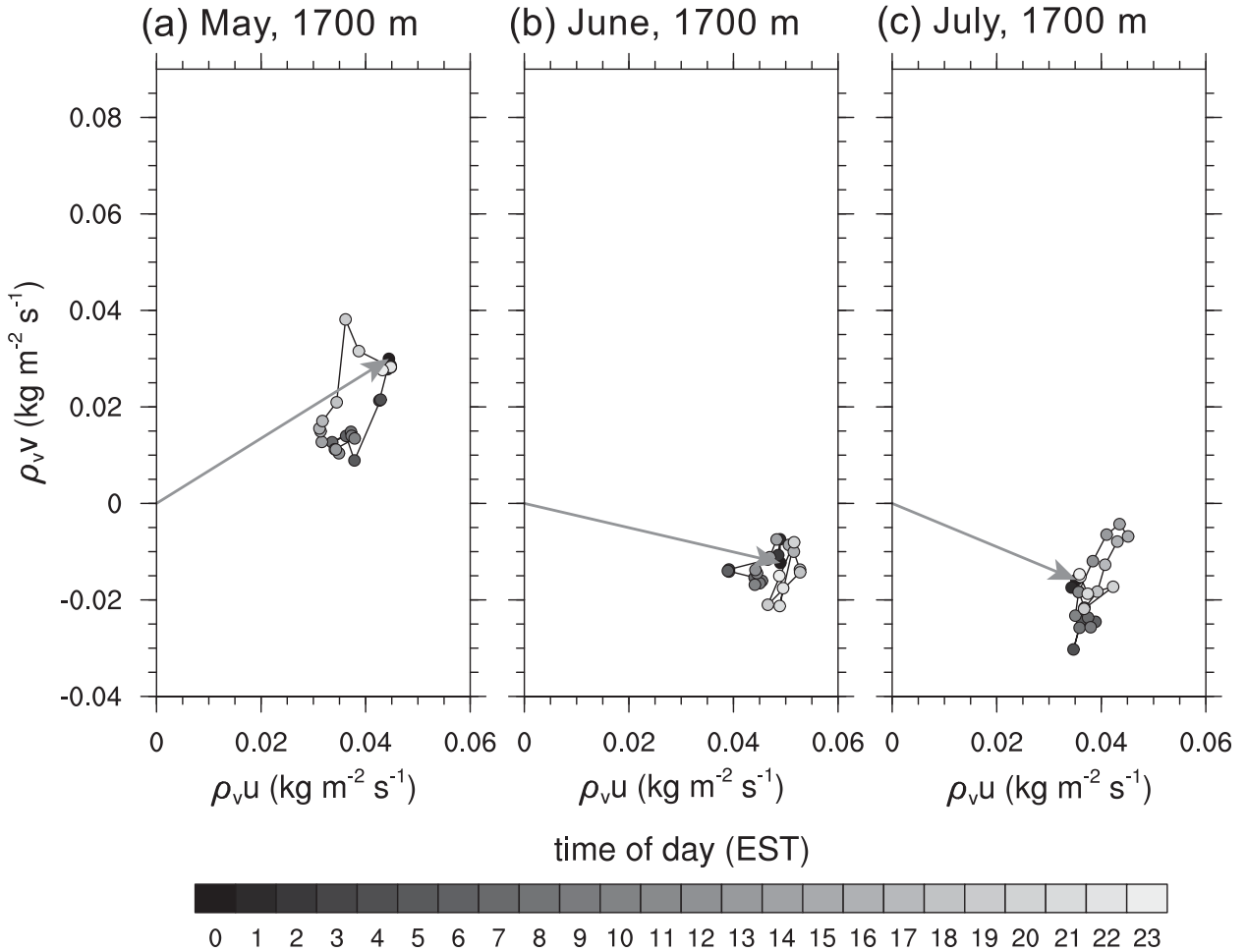


FIG. 13. As in Fig. 12, but for 1.7 km AGL.

(southeastward) upper-level winds are also observed in May (June and July).

In the mid-Atlantic region, winds at 850-hPa are nearly eastward during May but become southeastward during June and July, as seen from monthly mean 850-hPa wind and geopotential height fields (Fig. 14) obtained from NARR. The change in strength of meridional wind in the mid-Atlantic region is strongly associated with the westward extension of the North Atlantic subtropical high (hereafter, the Bermuda high), as can be seen in 850-hPa geopotential height fields. Under the influence of the Bermuda high, the mid-Atlantic region in summer experiences southeastward flow. Therefore, the large-scale flow in summer (i.e., the southward component) is opposite to the low-level northward flow that appears during afternoon and evening hours.

Composites of 850-hPa wind and geopotential height under nonprecipitation conditions and precipitation conditions more clearly show the influence of high pressure systems (Figs. 15, 16). A precipitation day is

defined as a day in which daily precipitation averaged over the area marked in Fig. 1 is greater or equal to 0.5 mm day^{-1} . The gridded hourly precipitation data used are the National Centers for Environmental Prediction (NCEP) stage IV data. Under the nonprecipitation conditions in which little precipitation is observed over the large area ($\sim 400 \text{ km} \times 550 \text{ km}$), the weather is likely influenced by high pressure systems, as can be seen in Fig. 15. Thus, it can be expected that the water vapor from the Gulf of Mexico is likely transported farther north to the mid-Atlantic region by the prevailing northeastward winds. In the mid-Atlantic region, the southeastward winds prevail under nonprecipitation conditions, which are located to the east of the ridge of high pressure systems in May, June, and July. Under precipitation conditions, 850-hPa winds become more eastward in the study region. In summer, a trough is observed along the eastern coast of the mid-Atlantic region and the 850-hPa winds are correspondingly east-southeastward. Thus, the mid-Atlantic

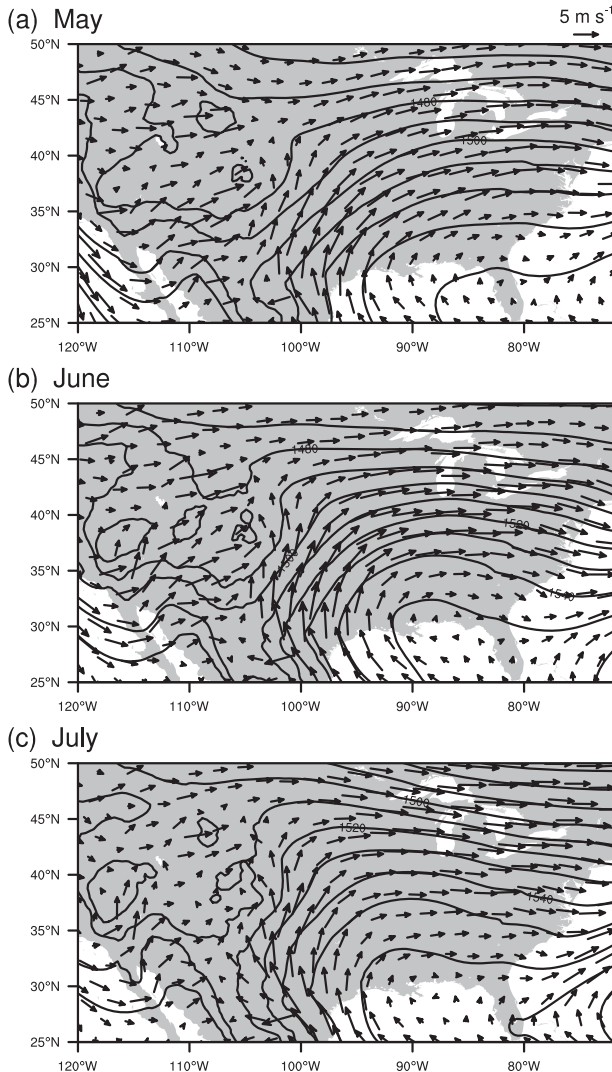


FIG. 14. Mean 850-hPa wind and geopotential height fields derived from NARR for 2007–12 in (a) May, (b) June, and (c) July.

region under precipitation conditions likely experiences direct transport of water vapor from the Gulf of Mexico.

During May, under nonprecipitation conditions, strong northward transport of water vapor appears at 0.35 km AGL at 2315 EST with a maximum of $0.095 \text{ kg m}^{-2} \text{ s}^{-1}$ (Fig. 17). Under precipitation conditions, the northward water vapor flux is observed in a 3-km layer over the entire day, and the large-scale flow under these conditions is responsible to some extent for the northward transport of water vapor. During 1900–2345 EST, the low-level transport is stronger under nonprecipitation conditions than under precipitation conditions. On the other hand, the low-level transport during 0000–0400 EST is stronger under precipitation

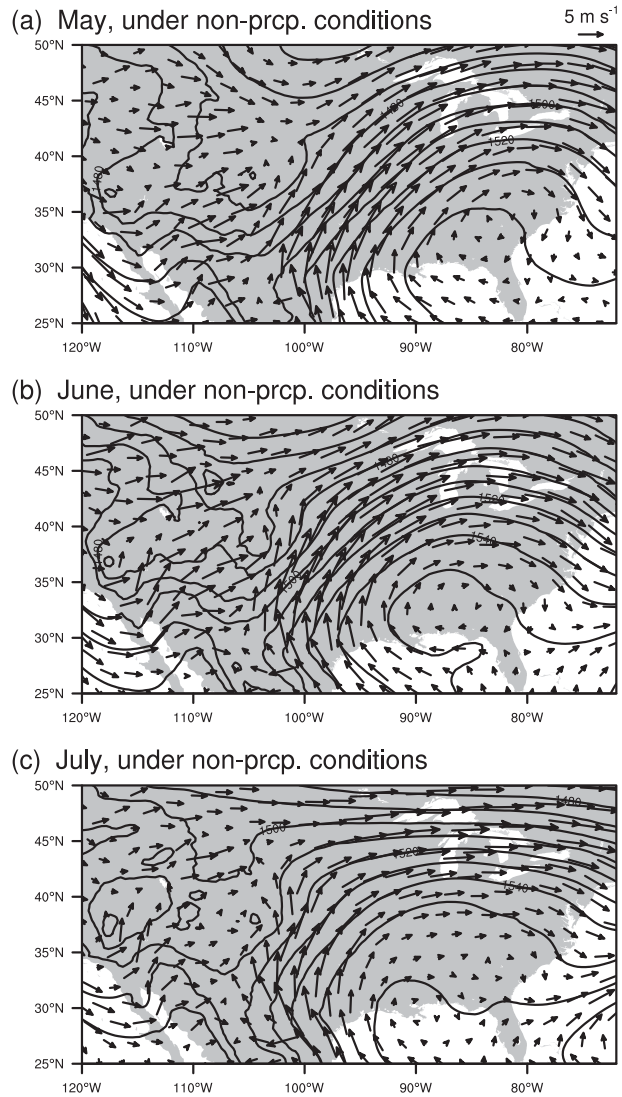


FIG. 15. As in Fig. 14, but for nonprecipitation conditions.

conditions. Similarly, during June and July, a stronger northward transport at low levels is observed at late times of day under nonprecipitation conditions than under precipitation conditions. While the northward water vapor flux at low levels reaches a peak at around 2300 EST under nonprecipitation conditions, it reaches a peak at an earlier time (around 2000 EST) under precipitation conditions.

4. Discussion

It is observed that during May strong northeastward transport of water vapor appears at low levels during nighttime hours and that during June and July relatively weak northeastward transport appears during afternoon and evening hours. Compared with previous studies that

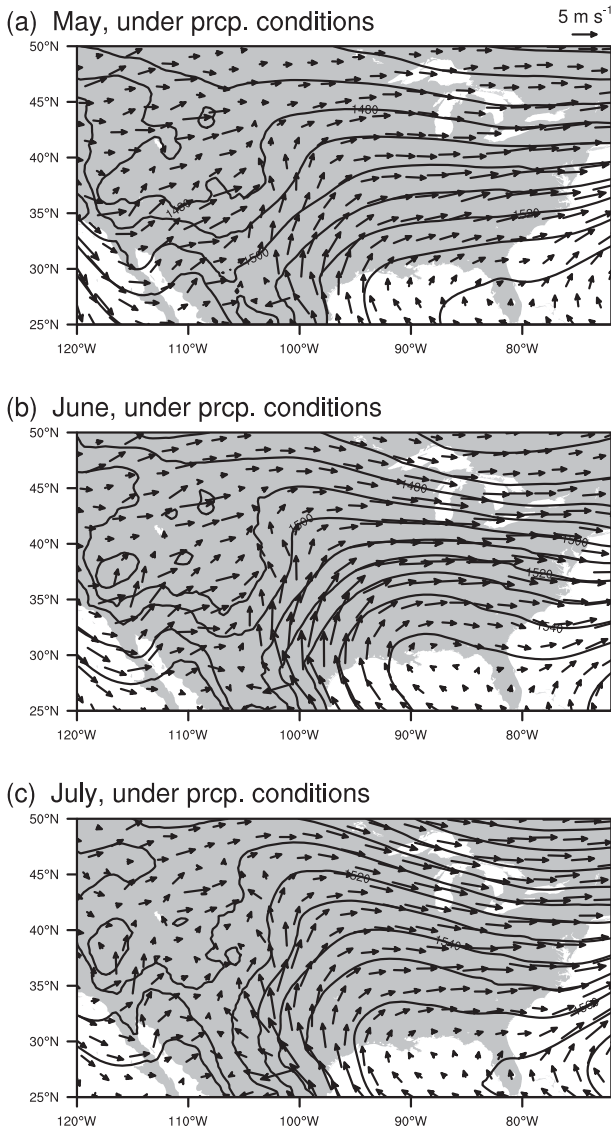


FIG. 16. As in Fig. 14, but for precipitation conditions.

investigated low-level jets in the mid-Atlantic region (e.g., Colle and Novak 2010; Zhang et al. 2006) or in other regions (e.g., Whiteman et al. 1997), these findings deviate from the general characteristics of low-level jets that occur more frequently in summer. Colle and Novak (2010), for example, showed that the New York Bight jets develop most frequently in June and July and that the distribution skews toward the spring months. However, they focused on low-level jets and defined jet occurrence using rigorous criteria. Although a direct comparison of its seasonal frequency of occurrence is not feasible because low-level jets are not rigorously dealt with in the present study, the less frequent and weaker northward component of low-level winds in summer can be attributed to some extent to the

transition of large-scale flow environments in the mid-Atlantic region between spring and summer seasons. So, in terms of large-scale flow conditions, this assertion is consistent with the finding of Colle and Novak (2010) that the northward New York Bight jet occurs on days with northeastward synoptic flow.

Such a seasonal transition of diurnal variation in water vapor flux is also seen in NARR fields. Figure 18 compares the time–height cross sections of meridional water vapor flux in May, June, and July obtained from the observations with those obtained from NARR. Although the magnitude of meridional water vapor flux from NARR is much smaller than that from the observations, it is clearly seen that the meridional water vapor flux from NARR shows similar diurnal variation to that from the observations in May, June, and July. In particular, the stronger northward flux during the evening hours in May than in June and July and also the southward flux at upper levels ($z > \sim 1.5$ km) in June and July are consistent with our findings from the observations. However, NARR fields do not show the enhanced low-level transport of water vapor from the south that is seen in the observations. It is found that the underestimated low-level transport from NARR is mainly due to the underestimated northward winds rather than water vapor density (not shown). The relatively coarse vertical resolution of NARR, which is approximately 200–250 m below 850-hPa level, could be responsible to some extent for the discrepancy at low levels.

In Fig. 17, it is observed that the difference in meridional water vapor flux between the late evening hours and the predawn hours is larger under nonprecipitation conditions than under precipitation conditions for all three months. This implies that the difference in horizontal temperature gradient between day- and nighttime, which is large under nonprecipitation conditions because of high pressure systems, can play some roles in increasing the amplitude of the oscillation. As Bonner and Paegle (1970) pointed out, a diurnally varying geostrophic wind due to baroclinicity can increase the amplitude of the oscillation that arises from a time-varying eddy viscosity alone. In a similar manner, the largest amplitude of the oscillation in May among the three months, which is seen in both the observations and NARR, can be to some extent due to the strong baroclinicity over this region. As an example, Fig. 19 shows the mean diurnal variation in temperature difference between Sterling and a point over the ocean (denoted A in Fig. 1) for the period of 2007–12. The temperature used is the NARR 1000-hPa temperature. The daytime temperature difference between land and sea is largest in May among the warm months. So, it is speculated that in addition to the northeastward winds prevailing in spring, the large amplitude of thermal wind

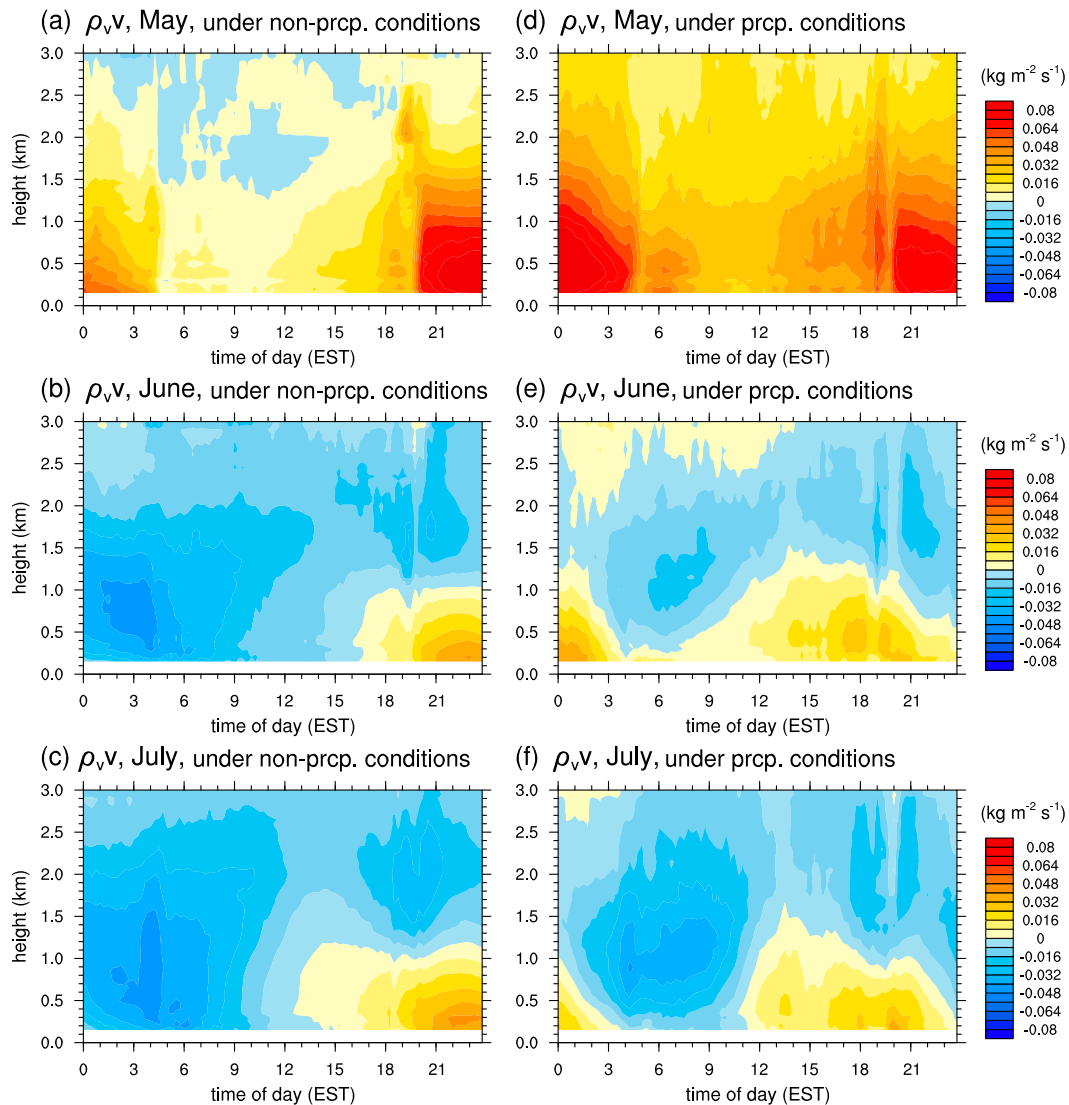


FIG. 17. Time–height cross section of meridional water vapor flux under (left) nonprecipitation and (right) precipitation conditions in (a),(d) May; (b),(e) June; and (c),(f) July.

oscillation resulting from the large horizontal temperature difference could lead to the large amplitude of the oscillation in low-level water vapor flux.

Our present study can be extended to further studies of water vapor flux in the mid-Atlantic region. For example, it can be applied to examine influences of diurnally varying water vapor transport on the diurnal cycles of precipitation in the mid-Atlantic region, as was done by Higgins et al. (1997) for the Great Plains. They showed that the low-level jets over the Great Plains have a considerable impact on the distribution and the intensity of nighttime precipitation. A numerical model can be used for examining the roles of low-level jets and local circulations on the transport of water vapor in the mid-Atlantic region in a more

systematic way. In addition, the roles of topography and land–sea contrast can also be understood, as was similarly done by Zhang et al. (2006) for the nocturnal low-level jets in the mid-Atlantic region.

5. Summary and conclusions

In this study, we present a new method for computing the vertically integrated water vapor flux using GPS precipitable water observations, VAD wind profiles developed from WSR-88D velocity observations, and radiosonde observations. The precipitable water and water vapor flux analyses match well with analyses based on twice-a-day radiosonde observations and provide the capability for examining the diurnal cycles

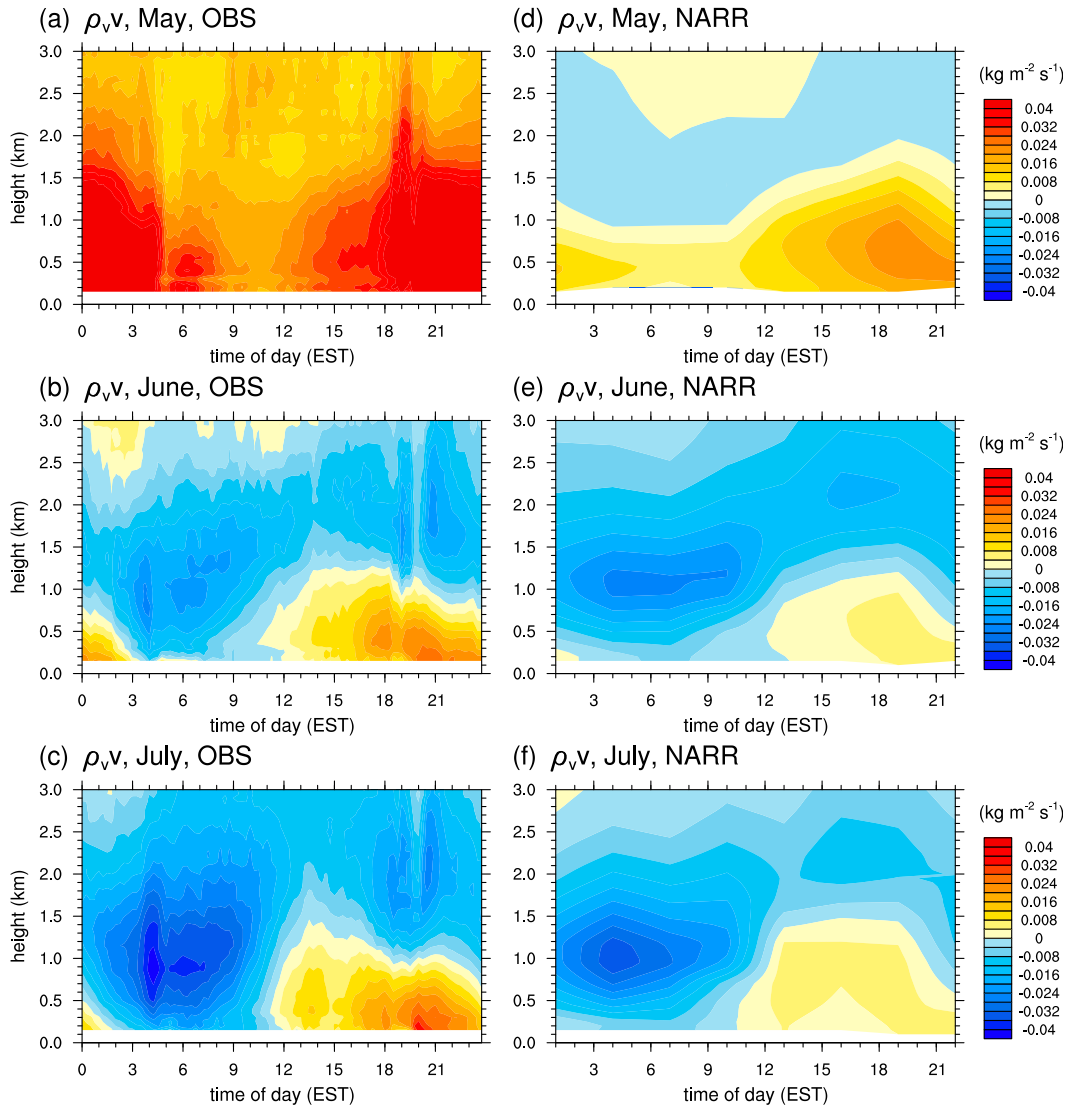


FIG. 18. Time–height cross section of meridional water flux from (left) observations and (right) NARR in (a),(d) May; (b),(e) June; and (c),(f) July.

of precipitable water and water vapor flux. The suggested method can further be used for studying the convergence/divergence of water vapor over a larger region.

Precipitable water in the mid-Atlantic region exhibits a pronounced seasonal cycle with median values ranging from a maximum of ~ 36 mm in July to a minimum of ~ 8 mm in January. The diurnal cycle of precipitable water, with an amplitude of ~ 1 mm in the mid-Atlantic region, is small compared to the seasonal cycle and to the diurnal cycle of water vapor flux.

The vertically integrated water vapor flux in the zonal direction peaks during June with median values of approximately $90 \text{ kg m}^{-1} \text{ s}^{-1}$; median values of zonal flux are positive for all months, indicating eastward transport

of water vapor in all seasons. The meridional water vapor flux has median values that are negative (southward transport) during the months of June–November and positive (northward transport) during the months of February–May. Seasonal variation of water vapor flux accelerates during May.

The diurnal cycle of water vapor flux during the summer is characterized by meridional transport with median values that are negative (southward transport) over the entire day. There is, however, significant diurnal variation in the meridional flux with median values ranging from $\sim -57 \text{ kg m}^{-1} \text{ s}^{-1}$ at 0700 EST to $\sim -6 \text{ kg m}^{-1} \text{ s}^{-1}$ at 1900 EST. By contrast, meridional transport of water vapor during spring has median values that are positive (northward transport) over the

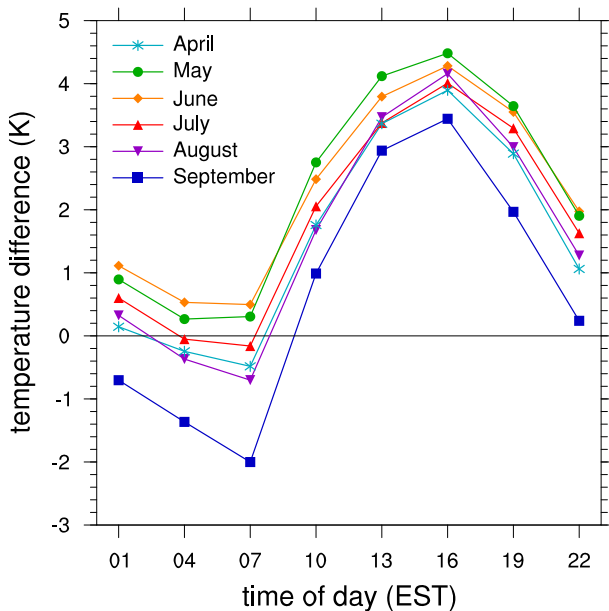


FIG. 19. Mean diurnal variation in difference in 1000-hPa temperature between Sterling and point A (marked in Fig. 1) in April–September for 2007–12.

entire day. Zonal water vapor flux is always dominated by eastward transport over the diurnal cycle during all seasons. During May, there is strong northward transport in the lowest 1 km of the atmosphere at night and weak northward transport during the middle of the day. During June and July, the diurnal cycle changes rapidly to a setting in which southward transport dominates below 1.5 km during the night and northward transport dominates below 1 km during the afternoon.

Mean hodographs of water vapor flux illustrate the diurnal oscillation at low levels and the rapid changes in diurnal cycle of water vapor transport during the May–July period. Temperature gradients between land and ocean, which peak during May for the mid-Atlantic region, could play a role in controlling seasonal and diurnal variation of water vapor flux through thermal wind oscillations.

Water vapor flux properties in the mid-Atlantic region differ substantially for precipitation and nonprecipitation days. Composite analyses of 850-hPa wind and geopotential height fields from NARR fields highlight contrasting flow environments between these important flow environments. Water vapor flux analyses based on NARR fields reflect some of the diurnal and seasonal properties of the vertical profile of water vapor flux. There are also significant contrasts that should be examined for climatological analyses of the water cycle based on NARR and other reanalysis products.

Acknowledgments. The authors thank Mary Lynn Baeck for assistance in acquiring data and for her helpful comments. The authors thank two anonymous reviewers for providing valuable comments on this work. The authors would like to acknowledge support for this research from the National Science Foundation (Grants EEC-0540832 and CBET-1058027) and the NOAA Cooperative Institute for Climate Science.

REFERENCES

- Baas, P., F. C. Bosveld, H. K. Baltink, and A. A. M. Holtslag, 2009: A climatology of nocturnal low-level jets in Cabauw. *J. Appl. Meteor. Climatol.*, **48**, 1627–1642, doi:10.1175/2009JAMC1965.1.
- Benton, G. S., and M. A. Estoque, 1954: Water-vapor transfer over the North American continent. *J. Meteor.*, **11**, 462–477, doi:10.1175/1520-0469(1954)011<0462:WVTOTN>2.0.CO;2.
- Bevis, M., S. Businger, S. Chiswell, T. A. Herring, R. A. Anthes, C. Rocken, and R. Ware, 1994: GPS meteorology: Mapping zenith wet delays onto precipitable water. *J. Appl. Meteor.*, **33**, 379–386, doi:10.1175/1520-0450(1994)033<0379:GMMZWD>2.0.CO;2.
- Blackadar, A. K., 1957: Boundary layer wind maxima and their significance for the growth of nocturnal inversions. *Bull. Amer. Meteor. Soc.*, **38**, 283–290.
- Bonner, W. D., and J. Paegle, 1970: Diurnal variations in boundary layer winds over the south-central United States in summer. *Mon. Wea. Rev.*, **98**, 735–744, doi:10.1175/1520-0493(1970)098<0735:DVIBLW>2.3.CO;2.
- Burk, S. D., and W. T. Thompson, 1996: The summertime low-level jet and marine boundary layer structure along the California coast. *Mon. Wea. Rev.*, **124**, 668–686, doi:10.1175/1520-0493(1996)124<0668:TSLLJA>2.0.CO;2.
- Colle, B. A., and D. R. Novak, 2010: The New York Bight jet: Climatology and dynamical evolution. *Mon. Wea. Rev.*, **138**, 2385–2404, doi:10.1175/2009MWR3231.1.
- Dai, A., and J. Wang, 2002: Diurnal variation in water vapor over North America and its implications for sampling errors in radiosonde humidity. *J. Geophys. Res.*, **107**, 4090, doi:10.1029/2001JD000642.
- Doyle, J. D., and T. T. Warner, 1991: A Carolina coastal low-level jet during GALE IOP 2. *Mon. Wea. Rev.*, **119**, 2414–2428, doi:10.1175/1520-0493(1991)119<2414:ACCLLJ>2.0.CO;2.
- Hanesiak, J., M. Melsness, and R. Raddatz, 2010: Observed and modeled growing-season diurnal precipitable water vapor in south-central Canada. *J. Appl. Meteor. Climatol.*, **49**, 2301–2314, doi:10.1175/2010JAMC2443.1.
- Held, I. M., and B. J. Soden, 2006: Robust responses of the hydrological cycle to global warming. *J. Climate*, **19**, 5686–5699, doi:10.1175/JCLI3990.1.
- Higgins, R. W., Y. Yao, E. S. Yarosh, J. E. Janowiak, and K. C. Mo, 1997: Influence of the Great Plains low-level jet on summertime precipitation and moisture transport over the central United States. *J. Climate*, **10**, 481–507, doi:10.1175/1520-0442(1997)010<0481:IOTGPL>2.0.CO;2.
- Mesinger, F., and Coauthors, 2006: North American Regional Reanalysis. *Bull. Amer. Meteor. Soc.*, **87**, 343–360, doi:10.1175/BAMS-87-3-343.
- Rasmusson, E. M., 1967: Atmospheric water vapor transport and the water balance of North America: Part I. Characteristics of the water vapor flux field. *Mon. Wea. Rev.*, **95**, 403–426, doi:10.1175/1520-0493(1967)095<0403:AWVTAT>2.3.CO;2.

- Sjostedt, D. W., J. T. Sigmon, and S. J. Colucci, 1990: The Carolina nocturnal low-level jet: Synoptic climatology and a case study. *Wea. Forecasting*, **5**, 404–415, doi:[10.1175/1520-0434\(1990\)005<0404:TCNLLJ>2.0.CO;2](https://doi.org/10.1175/1520-0434(1990)005<0404:TCNLLJ>2.0.CO;2).
- Wang, J., L. Zhang, A. Dai, T. V. Hove, and J. V. Baelen, 2007: A near-global, 2-hourly data set of atmospheric precipitable water from ground-based GPS measurements. *J. Geophys. Res.*, **112**, D11107, doi:[10.1029/2006JD007529](https://doi.org/10.1029/2006JD007529).
- Whiteman, C. D., X. Bian, and S. Zhong, 1997: Low-level jet climatology from enhanced rawinsonde observations at a site in the southern Great Plains. *J. Appl. Meteor.*, **36**, 1363–1376, doi:[10.1175/1520-0450\(1997\)036<1363:LLJCFE>2.0.CO;2](https://doi.org/10.1175/1520-0450(1997)036<1363:LLJCFE>2.0.CO;2).
- Wu, P., J.-I. Hamada, S. Mori, Y. I. Tauhid, and M. D. Yamanaka, 2003: Diurnal variation of precipitable water over a mountainous area of Sumatra Island. *J. Appl. Meteor.*, **42**, 1107–1115, doi:[10.1175/1520-0450\(2003\)042<1107:DVOPWO>2.0.CO;2](https://doi.org/10.1175/1520-0450(2003)042<1107:DVOPWO>2.0.CO;2).
- Zhang, D.-L., S. Zhang, and S. J. Weaver, 2006: Low-level jets over the mid-Atlantic states: Warm-season climatology and a case study. *J. Appl. Meteor. Climatol.*, **45**, 194–209, doi:[10.1175/JAM2313.1](https://doi.org/10.1175/JAM2313.1).